ARTICLE

Direct Imaging of Long-Range Exciton Transport in Quantum Dot Superlattices by Ultrafast Microscopy

Seog Joon Yoon,[†,‡] Zhi Guo,[§] Paula C. dos Santos Claro,[∥] Elena V. Shevchenko,[∥] and Libai Huang[*,§]

[†]Radiation Laboratory, University of Notre Dame, Notre Dame, Indiana 46556, United States
[‡]Department of Chemistry and Biochemistry, University of Notre Dame, Notre Dame, Indiana 46556, United States
[§]Department of Chemistry, Purdue University, West Lafayette, Indiana 47907, United States
[∥]Center for Nanoscale Materials, Argonne National Laboratory, Argonne, Illinois 60439, United States

Ⓢ *Supporting Information*

ABSTRACT: Long-range charge and exciton transport in quantum dot (QD) solids is a crucial challenge in utilizing QDs for optoelectronic applications. Here, we present a direct visualization of exciton diffusion in highly ordered CdSe QDs superlattices by mapping exciton population using ultrafast transient absorption microscopy. A temporal resolution of ~200 fs and a spatial precision of ~50 nm of this technique provide a direct assessment of the upper limit for exciton transport in QD solids. An exciton diffusion length of ~125 nm has been visualized in the 3 ns experimental time window and an exciton diffusion coefficient of $(2.5 \pm 0.2) \times 10^{-2}$ cm² s⁻¹ has been measured for superlattices constructed from 3.6 nm CdSe QDs with center-to-center distance of 6.7 nm. The measured exciton diffusion constant is in good agreement with Förster resonance energy transfer theory. We have found that exciton diffusion is greatly enhanced in the superlattices over the disordered films with an order of magnitude higher diffusion coefficient, pointing toward the role of disorder in limiting transport. This study provides important understandings on energy transport mechanisms in both the spatial and temporal domains in QD solids.

KEYWORDS: *energy transfer, femtosecond transient absorption spectroscopy, pump–probe microscopy, exciton diffusion, quantum dot solids*

$D \text{ (exciton)} = 0.025 \text{ cm}^2\text{s}^{-1}$
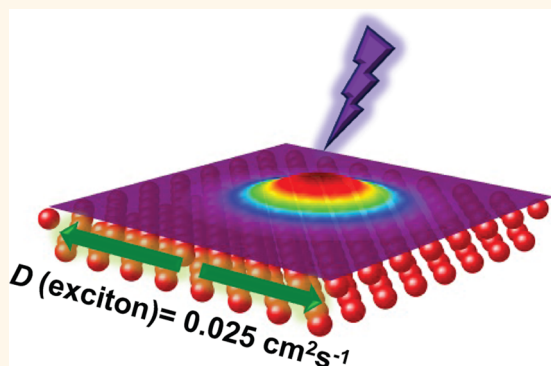
Colloidal semiconductor quantum dots (QDs) are highly efficient light absorbers and emitters, promising for a wide range of optoelectronic applications such as light emitting diodes,[1] photovoltaics,[2–4] and photodetectors.[5] Quantum confinement effects lead to strongly bound electron–hole pairs (i.e., excitons) with tunable emission covering the visible to infrared spectral range. The performance of many proposed optoelectronic applications relies not only on the properties of the individual QDs but also on the properties arising from interactions between the QDs in the solids.[6–8] For example, in solar cells, the ability to transport exciton or charge over long distances is required for achieving high efficiency in devices.[8–10] Therefore, a thorough understanding of mechanisms controlling long-range energy transport in QD solids is necessary for device designing. Although the photophysical properties of individual and dilute QDs systems (e.g., solutions) have been extensively investigated, understanding of the energy transport in QD solids is much less established.

Interparticle distances play an important role in governing energy and charge transfer rates in QD assemblies. When interparticle distances are between 1–10 nm, Förster resonance energy transfer (FRET) mechanism is used to describe energy transfer between QDs.[11–18] FRET predicts the energy transfer rate is strongly dependent on interparticle distance, with a $1/R^6$ dependence, where R is the distance between the particles. Although energy transfer has been investigated in QD solids,[11–19] these studies have been carried out exclusively in disordered arrays with a distribution of both particle size and interparticle distance. Such disorder can create energetic traps that slow down transport.[8] Also, as first shown by Anderson,[20] disorder provides interference effects to the diffusion of the electronic wave function (Anderson localization).[20–22] There-

 A

fore, conducting research of the charge/energy transport in ordered arrays, where both particle size and interparticle distance are well-defined, is essential to further elucidate mechanisms.[22,23] Despite the impressive progress made in fabrication of highly ordered QD superlattices allowing assembly of microsized 3D crystals using QDs as "artificial atoms",[10,15,24] obtaining a comprehensive picture of energy transport in QD solids remains a challenge due to the lack of measuring exciton diffusion directly. The most widely applied indirect method to measure exciton diffusion is based on photoluminescence (PL) quenching.[19] More recently, time-resolved PL microscopy has been applied to image exciton diffusion in disordered QD solids.[18] However, PL based methods are limited to ~100 ps time resolution, insufficient to resolve energy and charge transfer processes that could occur on the picosecond or shorter time scales. Transient absorption based imaging techniques with subpicosecond temporal resolution have been applied to image charge and plasmon propagation.[25−27] We have recently developed ultrafast transient absorption microscopy (TAM) with 50 nm spatial precision and 200 fs temporal resolution as a means to directly image exciton and charge populations in space and in time.[28,29]

In the present work, we use CdSe QD superlattice as a model system to investigate exciton transport mechanisms and to assess the upper-limit of exciton transport in QD solids. We directly image exciton population in both spatial and temporal domains using TAM with a temporal resolution of 200 fs and a spatial precision of ~50 nm. An exciton diffusion length of ~125 nm has been visualized for the 3 ns experimental time window and an exciton diffusion constant of 0.025 $cm^2 s^{-1}$ has been directly measured for QD superlattices. Our measurements show that FRET is sufficient in describing exciton transport at large interparticle distances. Exciton diffusion coefficient is about an order of magnitude larger in the highly ordered superlattice than the value obtained for disordered arrays implying disorder plays an important role in limiting transport.

RESULTS AND DISCUSSION

Structural Properties of CdSe QD Superlattices. To obtain long-range ordered CdSe QD superlattices, it is necessary for the particles to have a well-formed crystalline core and a small size distribution so that the QDs are practically indistinguishable.[30] The diameter of CdSe QDs is 3.6 nm ±0.3 nm, determined from scanning transmission electron microscopy (STEM) images as shown in Figures S1a,b, in the Supporting Information (SI). The synthesis procedure adopted herein provides CdSe with a wurtzite structure[31] as confirmed by X-ray diffraction (Figure S1c) and high-resolution transmission electron microscopy (TEM) (Figure S1c, inset). More details on characterization of the QD size and structure can be found in the SI. It has been suggested that QDs packed with <1 nm interparticle separation may induce sintering, necking, or partial ripening, leading to increased disorder.[7] To avoid this complication, octadecylphosphonic acid (ODPA) was used as surface ligands herein, to control the interparticle distance with separations longer than 1 nm between QDs. Three types of samples are studied in this work: superlattices, disordered films formed by drop-casting, and colloidal solution. To make sure the surface and trap state densities are comparable in all samples, QDs were washed with ethanol three times to remove excessive surface ligand prior to growth of superlattices, drop-casting, and redissolving into toluene.

We grow micron-sized CdSe superlattices by following established procedure[10,32] and more details can be found in the SI. The optical micrograph of the superlattice investigated in this study is shown in the inset of Figure 1a (micrograph of
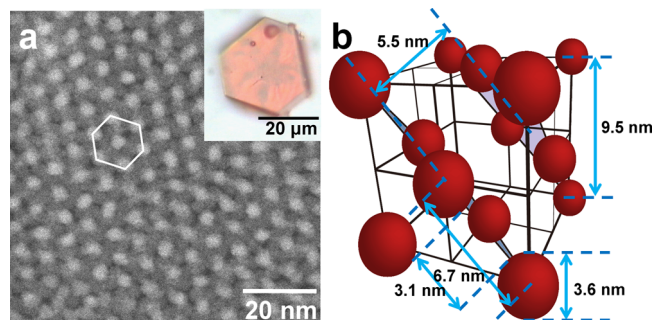

Figure 1. Structure of the superlattices. (a) STEM image of CdSe QDs packing on TEM grid (Inset: optical micrograph of a QD superlattice deposited on glass substrate). (b) Schematic illustration of the QD superlattice, packed as a cubic close packing structure. Diameter of QD, center-to-center distance edge-to-edge distance, interplanar distance of d_{111}, and lattice parameters are 3.6, 6.7, 3.1, 5.5, and 9.5 nm, respectively.

more superlattices in Figure S2). In order to image the arrangement of the QD in the superlattices, we use vacuum-assisted deposition to deposit CdSe QD superlattices on TEM grids (Scheme S1). As shown in the STEM image (Figure 1a), the surface particles correspond to the [111] projections of *fcc* lattice,[33] consistent with previous reports.[10,34] The *fcc* lattice of CdSe QD superlattices is also confirmed by small-angle X-ray scattering (SAXS, Figure S 1d). The analysis of the SAXS data reveals the center-to-center distance between adjacent QDs in the (111) plane to be 6.7 nm and the lattice constant of the superlattice unit cell to be 9.5 nm (more details on assignment in SI), consistent with the values measured from STEM images. The overall QD configuration in *fcc* superlattice is illustrated in Figure 1b.

Steady state UV−visible absorption and photoluminescence (PL) spectroscopy are applied to characterize the superlattice and compared with those from the colloidal QDs (Figure 2a). The absorption of CdSe QDs in colloidal solution shows distinct quantized energy levels: $1S-1S_{3/2}$ at 565 nm, $1S-2S_{3/2}$ at 541 nm, and $1P-2P_{3/2}$ at 470 nm, consistent with previous reports.[35] In the case of the superlattice, the absorption maximum of the first exciton is red-shifted to 568 nm, and the full width at half-maximum (fwhm) is broadened to 50 nm (36 nm for colloids), which can be explained by weak coupling of electronic states between the QDs.[22,24] The broadening and red shifting of the PL band has also been observed (Figure 2a). Note that in CdSe QD solids, the coupling energy is much smaller than the exciton binding energy and does not result in exciton dissociation.[6] Therefore, exciton remains to be the main form of photoexcitation in the CdSe QD superlattices and thin films.

Exciton Dynamics in Superlattices. We first employ ensemble transient absorption and time-resolved PL spectroscopy to investigate the exciton dynamics of CdSe QD superlattices. A disordered film formed by drop casting with similar optical density as the superlattice is used as a control. All samples were excited with a femtosecond pulse (387 nm, ~ 130 fs fwhm) and the transient absorption spectra of the sample were recorded between the spectral regime of 450−700 nm.
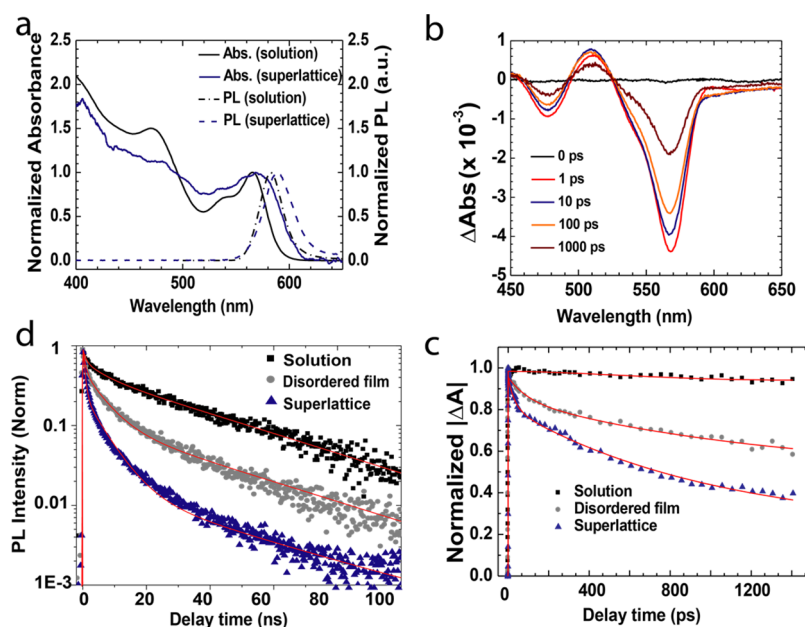
Figure 2. (a) UV–vis. absorption spectra and photoluminescence (PL) spectra of CdSe QD dispersed in toluene solution and in a single superlattice. (b) Time-resolved absorption spectra of CdSe QD superlattice by 387 nm laser pulse excitation (pump power density: 78 μJ/cm^2). (c) Transient absorption kinetic traces at bleach maximum for CdSe QDs in colloidal solution (probed at 566 nm, black square), disordered film (probed at 568 nm, silver sphere), and superlattice (probed at 568 nm, blue triangle), all with 387 nm laser pulse excitation (pump power density: 78 μJ/cm^2). (d) Time-resolved PL traces of CdSe QDs in colloidal solution (black square), in the disordered film (silver sphere), and in the superlattice (blue triangle) by 447 nm laser excitation with 10 nJ/cm^2 power intensity.

For the superlattice (Figure 2b), the colloidal solution (Figure S3), and the disordered film of CdSe QDs (Figure S3), three bleach bands around 570, 540, and 470 nm have been observed that correspond to the transitions in the ground-state absorption (Figure 2a).

The exciton dynamics of QDs in the colloidal solution serve as the baseline to understand the exciton dynamics in the superlattice. As shown in Figure 2d, the PL decay for the QDs in colloidal solution can be fitted to a triexponential decay function with decay constants of 0.9 ns (33%), 6 ns (21%), and 35 ns (46%). The multiexponential decay behavior in the colloidal QDs has been attributed to the fluctuations in nonradiative relaxation pathways at the single QD level.[36] The nonradiative pathways include quenching of the exciton by the charge or trap sites on the QD surface. The contribution of the subnanosecond component in PL lifetime increases from 33% (0.9 ns) for QDs in the solution to 77% (0.5 ns) in the superlattice, whereas contributions from the 6 and 35 ns components decrease in the superlattice. We further investigate the picosecond time scale dynamics using transient absorption spectroscopy (Figure 2c). When comparing the decay of the lowest 1S–1S$_{3/2}$ excitonic bleach around 570 nm, there is an additional fast relaxation for the superlattice with a time constant ~50 ps, which is absent for colloidal solutions. The PL decay of the disordered film (Figure 2d) is in between that of the superlattice and that of the colloidal solution, with the fast subnanosecond decay constant of 0.7 ns (61%). The fast decay component in the transient absorption dynamics of the disordered film is ~70 ps (Figure 2c).

The faster exciton decay in the superlattice and the disordered film compared to that in colloidal solution arises from the interaction between the QDs in the solids. A decrease in PL lifetimes has been previously reported for QD films when compared to colloidal QDs, which has been predominately

attributed to energy transfer between the neighboring QDs.[11−18] However, the donors and acceptors are nearly identical sized QDs in the superlattice, and energy transfer among the QDs alone should not deplete the exciton population until they are captured by defects. Instead, we attribute here the faster exciton decay in the QD superlattice to a faster exciton diffusion in the superlattice that allows for the excitons to sample more trap/defect sites on multiple QDs within their lifetime. In comparison, excitons can only access trap/defect sites on individual QDs in colloidal solutions. The fast components in the transient absorption and time-resolved PL measurements on the CdSe superlattice correspond to the time for the excitons to find a trap site. This assignment is consistent with the fact that red-shifted emission ~800 nm from the trap sites[37] is much more pronounced for the superlattice than for the colloidal solution (Figure S4) because more excitons can reach these sites. Exciton decay in the disordered film is faster than in colloidal solution but slower than in the superlattice, which agrees with the slower exciton diffusion in disordered solids as compared to ordered superlattices as discussed below. The faster energy transfer in the superlattice also leads to a lower PL quantum yield (QY) than the disordered film as shown in Figure S5.

Direct Imaging and Modeling of Exciton Transport. In order to investigate exciton diffusion directly, we employed pump–probe TAM to directly map exciton population in both spatial and temporal domains in the superlattice and the control disordered film. To image transport, the pump beam is held at a fixed position while the probe beam is scanned relative to the pump with a pair of galvanometer scanners to form an image (Scheme S2, more details in SI). The transmitted probe is collected and the pump-induced change in probe transmission ΔT is detected. Unlike the previous study based on PL,[18] TAM monitors all excited state population including those that do

not decay radiatively. This ability to monitor all population is important to capture the essential energy transfer pathways because majority of the excited population decays non-radiatively as manifested by the low QY (2% for colloidal solution). The pump wavelength is at 387 nm and the probe wavelength is chosen to be at 568 nm to monitor the bleach of the exciton resonance.

Figure 3a shows the 2D exciton density map as imaged by TAM at two pump−probe delay times measured on the flat
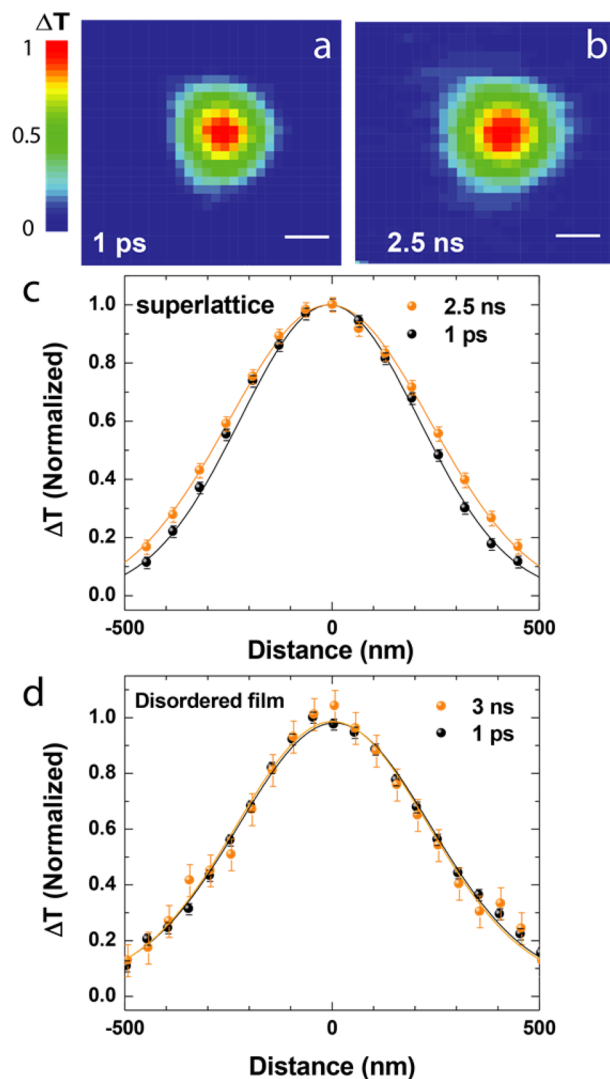
Figure 3. TAM imaging of exciton diffusion. Images formed by spatially scanning the probe beam relatively to the pump beam (pump power density: 3.2 μJ cm^{-2}) Scale bars: 300 nm. 2D normalized carrier density profiles distribution on $fcc(111)$ plane of the superlattice at two different time delays: 1 ps (a) and 2.5 ns (b). The transmission values ($\Delta T/T$) were normalized to the maxima at 1 ps. (c) Normalized 1D exciton density profiles of the superlattice fitted with Gaussian functions at two different delay times: 1 ps and 2.5 ns. (d) Normalized 1D exciton density profiles fitted of the disordered film at two different delay times: 1 ps and 3 ns.

$fcc(111)$ plane of the superlattice. The longest delay we can access is ~3 ns, which is limited by the length of our optical delay stage. At 1 ps, the normalized transmission ($\Delta T/T$) values represent the initial photogenerated exciton population by the pump beam (3.2 μJ cm^{-2}, ~ 1 exciton/160 QDs, using a

value of 0.9×10^{-15} cm^2 for absorption cross section).[38] As the delay time of probe beam increases, the distribution reflects exciton diffusion as well as recombination processes. Clear diffusion can be seen in the 2.5 ns TAM image for the superlattice (Figure 3c). In contrast, no diffusion is observed for the disordered film on the same time scale under similar experimental conditions as shown in Figure 3d. Please note that the population distributions in Figure 3c and 3d are normalized to the maximum ΔT at different delay times and the same population distributions plotted on absolute scales are shown in Figure S6. For a given excitation volume, most of the population is lost due to exciton decay and trapping, whereas exciton diffusion only contributes a small percentage to population loss (Figure S6).

To quantitatively model exciton transport, the exciton density profiles as shown in Figure 3c are fitted with Gaussian functions. At zero delay time, the pump beam at position (x_0, y_0) generates an initial population $n(x, y, 0)$, which can be approximated as a Gaussian function

$$n(x, y, 0) = N\exp\left[-\frac{(x - x_0)^2}{2\sigma(0)_x^2} - \frac{(y - y_0)^2}{2\sigma(0)_y^2}\right] \quad (1)$$

The pump and probe beam sizes are ~250 nm and ~210 nm, respectively. The population distribution at any later time t can also be described by a Gaussian function as long as there is no spatial dependence on exciton transport (i.e., no spatial variation in the structure, which is the case for the superlattice)

$$n(x, y, t) = N\exp\left[-\frac{(x - x_0)^2}{2\sigma(t)_x^2} - \frac{(y - y_0)^2}{2\sigma(t)_y^2}\right] \quad (2)$$

The CdSe QDs are spherical and ordered in the $fcc[111]$ projection, so the exciton diffusion is expected to be isotropic over all three dimensions in the superlattices. Because exciton diffusion along different directions (x, y, and z) is independent and has identical rates,[18] the exciton diffusion coefficients can be measured in the x−y plane by integrating over the z direction. Thus, the TAM images as shown in Figure 3 integrate all exciton density in the z direction, and the analysis is reduced to a two-dimensional exciton diffusion problem. Because the diffusion coefficients along the x and along the y direction are identical, we can further reduce exciton transport to one-dimension (1D)[18] by taking 1D cross sections of the two-dimensional exciton density maps as shown in Figure 3c or directly image transport in 1D (Figure 4a).

When the exciton density profiles are described by Gaussian functions, the exciton transport length L at delay time t is related to the variance (σ) of the exciton density profile

$$L^2 = \sigma(t)^2 - \sigma(0)^2 \quad (3)$$

L is ~125 nm for the 3 ns time window and under the excitation intensities of our experiments. $\sigma(t)^2 - \sigma(0)^2$ at different pump−probe delays obtained from the 1D line scans are presented in Figure 4a. As a control, results from the disordered film are also plotted. The precision in determining the exciton propagation distance L is dictated by the smallest measurable change in the population profiles, and not directly by the diffraction limit as described in the SI. The probe beam size does not change as a function of pump−probe delay (Figure S7), which indicates that no experimental artifact is induced by scanning the probe beam by an optical delay stage
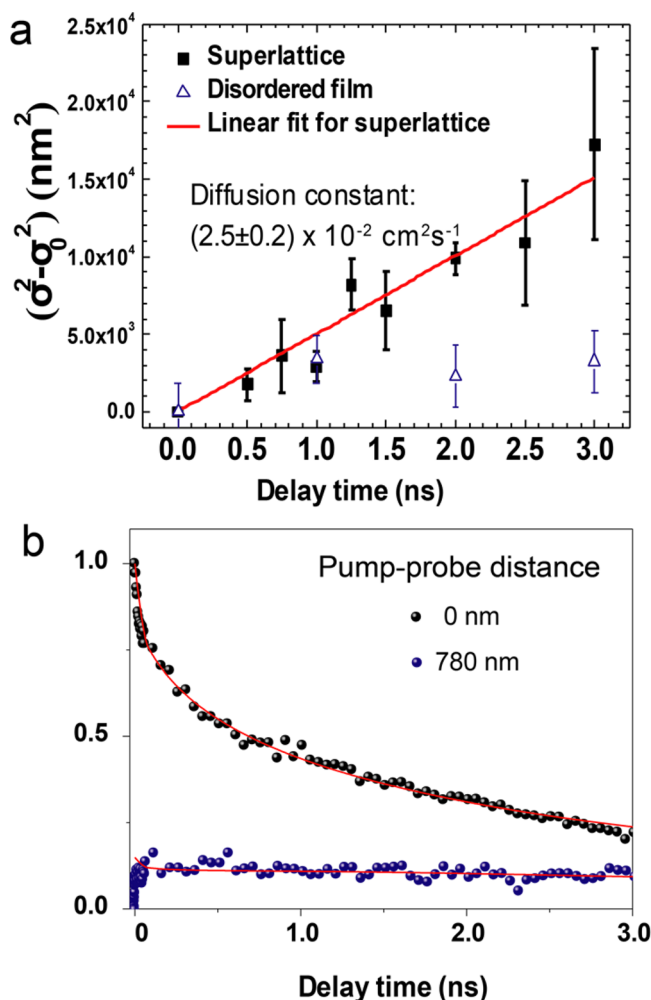
Figure 4. Analysis of exciton transport. (a) The time evolution of $\sigma(t)^2 - \sigma(0)^2$ measured by TAM and diffusion coefficient D calculated using eq 5 for the superlattice. The diffusion coefficient was obtained on the $fcc(111)$ plane of the superlattice. As a control, results from the disordered film are also plotted. (b) Exciton decay traces taken when the probe beam is spatially overlapped with the pump beam (black) and 780 nm away from the position of pump beam (blue). Both traces are fitted using the diffusion model as described by eq 6.

respective to the pump beam. We estimate the uncertainty in our experiments by taking the average of five different measurements at each pump−probe delay time and present the error bars as in Figure 4a. For the signal-to-noise ratio of our measurement, the precision in determining transport is ∼50 nm.

If the exciton transport is diffusive, exciton population can be described as diffusion out of the initial excitation volume coupled to exciton decay

$$\frac{\partial n(x, t)}{\partial t} = D\nabla^2 n(x, t) - kn(x, t) \tag{4}$$

where D is the diffusion constant and k is the exciton decay rate. For 1D solution, the solution of eq 4 gives the diffusion constant D as

$$D = \frac{\sigma(t)^2 - \sigma(0)^2}{2t} = \frac{L^2}{2t} \tag{5}$$

Therefore, $\sigma(t)^2 - \sigma(0)^2$ should scale linearly with pump−probe delay for normal diffusive transport as predicted by eq 5. The time evolution of $\sigma(t)^2 - \sigma(0)^2$ measured by TAM is plotted in Figure 4a. A linear relationship can be found indicative of diffusive exciton transport and a diffusion coefficient of $(2.5 \pm 0.2) \times 10^{-2}$ cm^2 s^{-1} is extracted by applying eq 5.

Because exciton annihilation could artificially broaden the exciton profile and lead to errors in determining the exciton diffusion coefficient, we have made sure that exciton annihilation does not play a role in the TAM measurements. Figure S8 illustrates the exciton−exciton annihilation threshold in the colloidal solution and the superlattice. Exciton−exciton annihilation is negligible at the pump intensity of 3.2 μJ cm^{-2} (∼1 exciton/160 QDs) for the TAM measurements. No obvious pump intensity dependent dynamics is observed until pump intensity is as high as 65 μJ cm^{-2} (∼1 exciton/6 QDs) for the superlattice. As shown in Figure S8, the exciton−exciton annihilation threshold for the superlattice of 60−80 μJ cm^{-2} (∼1 exciton/7 QDs) is similar as that for the colloidal solution of 78 μJ cm^{-2}, which is consistent with the threshold previously reported.[39] The similar threshold for the superlattice to that of the colloidal solution could be understood as following: excitons can diffuse in the superlattice and therefore reduces the probability of creating two excitons on the same QD, however, diffusion also allows excitons to encounter excitons originated on other QDs. Because energy transfer (∼50 ps) is roughly on the same time scale of exciton−exciton annihilation (∼300 ps),[39] these two effects somewhat cancel out and we do not observe a significant difference in exciton−exciton annihilation threshold for the superlattice and the colloidal solution.

Next, we simulate the spatial dependent dynamics using the diffusion modeled as described by eq 4. As shown in Figure 2, exciton decay is multiexponential in the superlattice. To account for the non monoexponential decay nature of the exciton decay, we use a time dependent exciton decay rate, $k(t)$. Equation 4 becomes

$$\frac{\partial n(x, t)}{\partial t} = D\nabla^2 n(x, t) - k(t)n(x, t) \tag{6}$$

We obtain the expression of $k(t)$ using the triexponential fitted trace from the ensemble transient absorption measurements as shown in Figure 2c. By using a D value of 2.5×10^{-2} cm^2 s^{-1} from the fit to eq 5, eq 6 is then numerically solved by evaluating the exciton distribution at each delay time step and probe position. Example of the simulation is shown in Figure 4b with kinetic traces at two different pump−probe distances simulated. Both simulated traces agree well with the dynamics measured experimentally. Therefore, the diffusion model can reproduce both the time dependent exciton density profiles and spatial dependent dynamics implying that exciton motion is indeed diffusive in the superlattice.

Comparing to FRET Theory. We compare the exciton diffusion rate measured experimentally to FRET theory. The center-to-center distance in the superlattice is 6.7 nm, which falls in the weak-coupling regime that should be sufficiently described by FRET.[40] Energy transfer rate k_{et} between the neighboring QDs is given by Fermi's golden rule[40]

$$k_{et} = \frac{2\pi}{\hbar}V^2 J \tag{7}$$

where V is the Coulomb coupling between donor and acceptor and J is spectral overlap. In the classical FRET theory, V is given by dipole−dipole approximation[40]

$$V^2 = \frac{\mu_D^2 \mu_A^2 \kappa^2}{R_{DA}^6 n^4} \tag{8}$$

where μ_D and μ_A and are the transition dipole moments of donor and acceptor QDs, R_{DA} is the distance between them, n is the refractive index of the medium (1.8 for ODPA ligands),[17] and κ^2 is orientation factor (2 for ordered dipole array).[32] We estimate the dipole moment to be $\mu_D = \mu_A = 20.3$ D (more details in the SI). Thus, V^2 is evaluated to be 8.5 cm^{-1}. The spectral overlap J is given by[40]

$$J = \int f_D(\lambda)\varepsilon_A(\lambda)\lambda^4 d\lambda \tag{9}$$

where λ is the wavelength, $f_D(\lambda)$ and $\varepsilon_A(\lambda)$ are the normalized emission spectrum of the donor and the extinction spectrum of the acceptor, respectively. In the case of the superlattice, the donor and acceptor are identical sized QDs. We use the experimentally measured absorption and PL spectrum as shown in Figure 2a to evaluate J to be 2×10^{-4} cm^{-1}. Combining eqs 7, 8, and 9, we obtain a value of (54 ps)$^{-1}$ for k_{et} using eq 7.

The diffusion constant D can be related to k_{et} and the distance between the donor and the acceptor R_{DA} by

$$D = k_{et}R_{DA}^2 \tag{10}$$

By using a R_{DA} value of 6.7 nm, a D of 0.9×10^{-2} cm^2 s^{-1} is predicted by classical FRET theory, which is on the same order of magnitude but about a factor of 3 smaller than the value measured experimentally by TAM. The factor of 3 is possibly due to the fact that the higher dipole coupling terms are ignored in the classical FRET model and/or the uncertainties in estimating V and J. The good agreement between our measurements and FRET implies that other factors such as energetic disorder play a negligible role in exciton transport highly ordered QD solids and the upper limit of exciton transport indeed can be achieved in superlattices over hundreds of nanometer distance.

Role of Disorder. Exciton diffusion is much faster in the superlattice than in the disordered film as seen in Figures 3 and 4. Clearly, diffusion is observed for superlattice in the 3 ns experimental time window, whereas no exciton diffusion is resolved for the disordered film with current resolution of ∼50 nm. The exciton diffusion coefficient for the superlattice measured here is almost two orders magnitude higher than the diffusion constant of 3×10^{-4} cm^2 s^{-1} reported by Akselrod et al. for disordered films.[18] After accounting for the differences in interparticle distance and orientation factor κ^2 (2 for super-lattices and 2/3 for disordered film), the D value is still about an order of magnitude higher in superlattices than in disordered solids. This points toward the importance in the role of disorder in limiting transport. We explain the enhanced exciton diffusion in the highly ordered QD superlattices by two factors. First, the distribution in QD sizes in disordered solids creates complex energy landscape where larger QDs with lower exciton energies function as energy sinks.[18] Second, the dispersive distribution in interparticle distance also creates hopping barriers due to large interparticle spacing that could slow down transport. These two factors have led to subdiffusive behavior in disordered QD solids.[18] In contrast, for super-lattices with well-defined QD size and interparticle distance,

disorder is small and the intrinsic limit for exciton transport can be achieved.

CONCLUSION

In summary, we directly image exciton transport in CdSe QD superlattices with ultrafast microscopy with a time resolution of ∼200 fs and a spatial precision of ∼50 nm. The spatially- and temporally resolved measurements reported here establish an important step toward discerning the underlying transport properties of QD solids. Most notably, our experiments measure an exciton diffusion coefficient of 2.5×10^{-2} cm^2 s^{-1} in the highly ordered superlattices, which is about an order of magnitude larger than disordered solids. FRET theory of incoherent exciton hopping successfully explains the exciton motion for the QD superlattice imaged in current study because the center-to-center distance is relatively large (6.7 nm). With shorter interparticle distance and ligand engineering, stronger interparticle coupling can lead to exciton delocaliza-tion over multiple QDs,[41−43] which could in principle lead to coherent mechanisms that do not require incoherent FRET hopping.[23,44,45] Femtosecond time resolution provide by TAM will be necessary for differentiating coherent and incoherent exciton transport. Further experiments on superlattices with shorter interparticle distance will be conducted to investigate how exciton delocalization enhances transport.

METHODS

Synthesis of CdSe QDs and Growth of CdSe QD Super-lattice. CdSe QDs were synthesized by a hot injection method.[31] The details of synthesizing CdSe QDs and growth of CdSe QD superlattice were described in the Supporting Information (SI). In short, CdO, trioctylphosphine oxide (TOPO), octadecene (ODE), and octadecyl-phosphonic acid (ODPA) were mixed and heated to 360 °C in inert atmosphere. Trioctylphosphine (TOP) and Se were mixed in glovebox and injected to the heated mixture, then the solution was cooled down and QDs were precipitated by dispersing in toluene and mixing with ethanol three times. To monitor packing behavior of CdSe QDs, colloidal QD solution was slowly evaporated on TEM grid (Scheme S1). To form superlattice on glass, CdSe QD colloidal solution in toluene, which has absorbance of 0.3 at 566 nm, was put in vial with the cover glass substrate. On top of the solution, nonsolvent (ethanol) was gently added. After the colloidal solution and nonsolvent have been slowly mixed for 3 days, QD superlattices can be formed on glass (Scheme S1b and Figure S2).

Structural and Optical Characterizations. Details on STEM, high-resolution TEM, SAXS measurements, steady-state optical measurements and time-resolved PL measurements are presented in the SI.

Transient Absorption Spectroscopy. Transient absorption spectra were recorded using a femtosecond laser system (Clark MXR CPA-2010, 130 fs pulse duration, 1 mJ/pulse output at 1 kHz repetition rate), with a transient absorption spectrometer (Ultrafast Systems). The 95% of fundamental frequency was converted to 387 nm using a frequency doubler to provide the pump beam. The remaining 5% was used to generate white light continuum as the probe beam by passing through a CaF$_2$ crystal. All CdSe QDs samples used for pump−probe measurements were sealed in glovebox beforehand.

Transient Absorption Microscopy. Detailed schematic config-uration of femtosecond transient absorption microscopy was described in Supporting Information (Scheme S2) and was reported earlier.[28] Briefly, a Ti:sapphire oscillator (Coherent Mira 900) pumped by a diode laser (Verdi V18) was used as the light source (output at 785 nm, 80 MHz repetition rate). The 70% of the pulse energy was used to pump an optical parametric oscillator (Coherent Mira OPO) to generate probe light at 568 nm, whereas the remainder 30% was doubled to 387 nm and serves as the pump beam. The repetition rate of both beams was reduced to 2.5 MHz using two clock-synchronized

pulse pickers (Model 9200, Coherent Inc.). The pump beam was modulated at 1 MHz using an acoustic optical modulator (AOM, model R21080-1DM, Gooch&Housego). A $60 \times$ NA = 1.49 objective (CFI Apo TIRF, Nikon Inc.) was used to focus the laser beams onto the sample, and the transmission light was then collected by another objective $(60 \times$ NA = 0.9) and detected by an avalanche photodiode (APD, Hamamatsu C5331-04). In exciton diffusion imaging, as shown in Figure 3, pump beam was fixed while the probe beam was scanned by a pair of Galvanometer mirrors (Thorlabs Inc.).

ASSOCIATED CONTENT

ⓢ Supporting Information

The Supporting Information is available free of charge on the ACS Publications website at DOI: 10.1021/acsnano.6b03700.

> Preparation of CdSe QDs and QD superlattice, material and photophysical characterization methods. Additional structural analysis of CdSe QD superlattices, TAM configuration and resolution, transition dipole calculation for CdSe QDs, and time-resolved transient absorption/PL spectra are also provided. (PDF)

AUTHOR INFORMATION

Corresponding Author
*E-mail: libai-huang@purdue.edu.

Author Contributions

(S.J.Y. and Z.G.) Equal contributors.

Notes

The authors declare no competing financial interest.

REFERENCES

(1) Bozyigit, D.; Yarema, O.; Wood, V. Origins of Low Quantum Efficiencies in Quantum Dot LEDs. *Adv. Funct. Mater.* **2013**, *23*, 3024−3029.

(2) Nozik, A. Quantum Dot Solar Cells. *Phys. E* **2002**, *14*, 115−120.

(3) Kamat, P. V. Quantum Dot Solar Cells. The Next Big Thing in Photovoltaics. *J. Phys. Chem. Lett.* **2013**, *4*, 908−918.

(4) Sargent, E. H. Colloidal Quantum Dot Solar Cells. *Nat. Photonics* **2012**, *6*, 133−135.

(5) Sukhovatkin, V.; Hinds, S.; Brzozowski, L.; Sargent, E. H. Colloidal Quantum-Dot Photodetectors Exploiting Multiexciton Generation. *Science* **2009**, *324*, 1542−1544.

(6) Choi, J. J.; Luria, J.; Hyun, B.-R.; Bartnik, A. C.; Sun, L.; Lim, Y.-F.; Marohn, J. A.; Wise, F. W.; Hanrath, T. Photogenerated Exciton Dissociation in Highly Coupled Lead Salt Nanocrystal Assemblies. *Nano Lett.* **2010**, *10*, 1805−1811.

(7) Guyot-Sionnest, P. Electrical Transport in Colloidal Quantum Dot Films. *J. Phys. Chem. Lett.* **2012**, *3*, 1169−1175.

(8) Kagan, C. R.; Murray, C. B. Charge Transport in Strongly Coupled Quantum Dot Solids. *Nat. Nanotechnol.* **2015**, *10*, 1013−1026.

(9) Chuang, C. H. M.; Brown, P. R.; Bulovic, V.; Bawendi, M. G. Improved Performance and Stability in Quantum Dot Solar Cells through Band Alignment Engineering. *Nat. Mater.* **2014**, *13*, 796−801.

(10) Talapin, D. V.; Lee, J. S.; Kovalenko, M. V.; Shevchenko, E. V. Prospects of Colloidal Nanocrystals for Electronic and Optoelectronic Applications. *Chem. Rev.* **2010**, *110*, 389−458.

(11) Baranov, A. V.; Ushakova, E. V.; Golubkov, V. V.; Litvin, A. P.; Parfenov, P. S.; Fedorov, A. V.; Berwick, K. Self-Organization of Colloidal PbS Quantum Dots into Highly Ordered Superlattices. *Langmuir* **2015**, *31*, 506−513.

(12) Crooker, S. A.; Hollingsworth, J. A.; Tretiak, S.; Klimov, V. I. Spectrally Resolved Dynamics of Energy Transfer in Quantum-Dot Assemblies: Towards Engineered Energy Flows in Artificial Materials. *Phys. Rev. Lett.* **2002**, *89*, 186802−186802.

(13) Bose, R.; McMillan, J. F.; Gao, J.; Rickey, K. M.; Chen, C. J.; Talapin, D. V.; Murray, C. B.; Wong, C. W. Temperature-Tuning of Near-Infrared Monodisperse Quantum Dot Solids at 1.5 μm for Controllable Forster Energy Transfer. *Nano Lett.* **2008**, *8*, 2006−2011.

(14) Lu, W.; Umezu, I.; Sugimura, A. Evolution of Energy Transfer Process between Quantum Dots of Two Different Sizes during the Evaporation of Solvent. *Jpn. J. Appl. Phys.* **2008**, *47*, 6592−6595.

(15) Kagan, C. R.; Murray, C. B.; Nirmal, M.; Bawendi, M. G. Electronic Energy Transfer in CdSe Quantum Dot Solids. *Phys. Rev. Lett.* **1996**, *76*, 1517−1520.

(16) Prins, F.; Sumitro, A.; Weidman, M. C.; Tisdale, W. A. Spatially Resolved Energy Transfer in Patterned Colloidal Quantum Dot Heterostructures. *ACS Appl. Mater. Interfaces* **2014**, *6*, 3111−3114.

(17) Mork, A. J.; Weidman, M. C.; Prins, F.; Tisdale, W. A. Magnitude of the Forster Radius in Colloidal Quantum Dot Solids. *J. Phys. Chem. C* **2014**, *118*, 13920−13928.

(18) Akselrod, G. M.; Prins, F.; Poulikakos, L. V.; Lee, E. M. Y.; Weidman, M. C.; Mork, A. J.; Willard, A. P.; Bulovic, V.; Tisdale, W. A. Subdiffusive Exciton Transport in Quantum Dot Solids. *Nano Lett.* **2014**, *14*, 3556−3562.

(19) Kholmicheva, N.; Moroz, P.; Bastola, E.; Razgoniaeva, N.; Bocanegra, J.; Shaughnessy, M.; Porach, Z.; Khon, D.; Zamkov, M. Mapping the Exciton Diffusion in Semiconductor Nanocrystal Solids. *ACS Nano* **2015**, *9*, 2926−2937.

(20) Lagendijk, A.; van Tiggelen, B.; Wiersma, D. S. Fifty Years of Anderson localization. *Phys. Today* **2009**, *62*, 24−29.

(21) Talgorn, E.; Gao, Y. N.; Aerts, M.; Kunneman, L. T.; Schins, J. M.; Savenije, T. J.; van Huis, M. A.; van der Zant, H. S. J.; Houtepen, A. J.; Siebbeles, L. D. A. Unity Quantum Yield of Photogenerated Charges and Band-Like Transport in Quantum-Dot Solids. *Nat. Nanotechnol.* **2011**, *6*, 733−739.

(22) Artemyev, M. V.; Bibik, A. I.; Gurinovich, L. I.; Gaponenko, S. V.; Woggon, U. Evolution from Individual to Collective Electron States in a Dense Quantum Dot Ensemble. *Phys. Rev. B: Condens. Matter Mater. Phys.* **1999**, *60*, 1504−1506.

(23) Ringsmuth, A. K.; Milburn, G. J.; Stace, T. M. Multiscale Photosynthetic and Biomimetic Excitation Energy Transfer. *Nat. Phys.* **2012**, *8*, 562−567.

(24) Murray, C. B.; Kagan, C. R.; Bawendi, M. G. Self-Organization of Cdse Nanocrystallites into 3-Dimensional Quantum-Dot Superlattices. *Science* **1995**, *270*, 1335−1338.

(25) Seo, M. A.; Yoo, J.; Dayeh, S. A.; Picraux, S. T.; Taylor, A. J.; Prasankumar, R. P. Mapping Carrier Diffusion in Single Silicon Core−Shell Nanowires with Ultrafast Optical Microscopy. *Nano Lett.* **2012**, *12*, 6334−6338.

(26) Lo, S. S.; Shi, H. Y.; Huang, L.; Hartland, G. V. Imaging the extent of plasmon excitation in Au nanowires using pump-probe microscopy. *Opt. Lett.* **2013**, *38*, 1265−1267.

(27) Gabriel, M. M.; Kirschbrown, J. R.; Christesen, J. D.; Pinion, C. W.; Zigler, D. F.; Grumstrup, E. M.; Mehl, B. P.; Cating, E. E. M.; Cahoon, J. F.; Papanikolas, J. M. Direct Imaging of Free Carrier and Trap Carrier Motion in Silicon Nanowires by Spatially-Separated

Femtosecond Pump—Probe Microscopy. *Nano Lett.* **2013**, *13*, 1336—1340.

(28) Guo, Z.; Manser, J. S.; Wan, Y.; Kamat, P. V.; Huang, L. B. Spatial and Temporal Imaging of Long-Range Charge Transport in Perovskite Thin Films by Ultrafast Microscopy. *Nat. Commun.* **2015**, *6*, 7471.

(29) Wan, Y.; Guo, Z.; Zhu, T.; Yan, S.; Johnson, J.; Huang, L. Cooperative Singlet and Triplet Exciton Transport in Tetracene Crystals Visualized by Ultrafast Microscopy. *Nat. Chem.* **2015**, *7*, 785—92.

(30) Murray, C. B.; Kagan, C. R.; Bawendi, M. G. Synthesis and Characterization of Monodisperse Nanocrystals and Close-Packed Nanocrystal Assemblies. *Annu. Rev. Mater. Sci.* **2000**, *30*, 545—610.

(31) Alam, R.; Zylstra, J.; Fontaine, D. M.; Branchini, B. R.; Maye, M. M. Novel Multistep BRET-FRET Energy Transfer Using Nano-conjugates of Firefly Proteins, Quantum Dots, and Red Fluorescent Proteins. *Nanoscale* **2013**, *5*, 5303—5306.

(32) Talapin, D. V.; Shevchenko, E. V.; Murray, C. B.; Titov, A. V.; Kral, P. Dipole-Dipole Interactions in Nanoparticle Superlattices. *Nano Lett.* **2007**, *7*, 1213—1219.

(33) Shevchenko, E. V.; Talapin, D. V.; Rogach, A. L.; Kornowski, A.; Haase, M.; Weller, H. Colloidal Synthesis and Self-Assembly of CoPt$_3$ Nanocrystals. *J. Am. Chem. Soc.* **2002**, *124*, 11480—11485.

(34) Bolhuis, P. G.; Frenkel, D.; Mau, S. C.; Huse, D. A. Entropy Difference Between Crystal Phases. *Nature* **1997**, *388*, 235—236.

(35) Klimov, V. I.; McBranch, D. W.; Leatherdale, C. A.; Bawendi, M. G. Electron and Hole Relaxation Pathways in Semiconductor Quantum Dots. *Phys. Rev. B: Condens. Matter Mater. Phys.* **1999**, *60*, 13740—13749.

(36) Fisher, B. R.; Eisler, H.-J.; Stott, N. E.; Bawendi, M. G. Emission Intensity Dependence and Single-Exponential Behavior In Single Colloidal Quantum Dot Fluorescence Lifetimes. *J. Phys. Chem. B* **2004**, *108*, 143—148.

(37) Dabbousi, B. O.; Rodriguez-Viejo, J.; Mikulec, F. V.; Heine, J. R.; Mattoussi, H.; Ober, R.; Jensen, K. F.; Bawendi, M. G. (CdSe)ZnS Core—Shell Quantum Dots: Synthesis and Characterization of a Size Series of Highly Luminescent Nanocrystallites. *J. Phys. Chem. B* **1997**, *101*, 9463—9475.

(38) Parson, W. W. *Modern Optical Spectroscopy*; Springer: New York, 2007.

(39) Klimov, V.; Mikhailovsky, A.; McBranch, D.; Leatherdale, C.; Bawendi, M. Quantization of Multiparticle Auger Rates in Semiconductor Quantum Dots. *Science* **2000**, *287*, 1011—1013.

(40) Curutchet, C.; Franceschetti, A.; Zunger, A.; Scholes, G. D. Examining Förster Energy Transfer for Semiconductor Nanocrystalline Quantum Dot Donors and Acceptors. *J. Phys. Chem. C* **2008**, *112*, 13336—13341.

(41) Crisp, R. W.; Schrauben, J. N.; Beard, M. C.; Luther, J. M.; Johnson, J. C. Coherent Exciton Delocalization in Strongly Coupled Quantum Dot Arrays. *Nano Lett.* **2013**, *13*, 4862—4869.

(42) Jin, S.; Harris, R. D.; Lau, B.; Aruda, K. O.; Amin, V. A.; Weiss, E. A. Enhanced Rate of Radiative Decay in CdSe Quantum Dots upon Adsorption of an Exciton-Delocalizing Ligand. *Nano Lett.* **2014**, *14*, 5323—5328.

(43) Straus, D. B.; Goodwin, E. D.; Gaulding, E. A.; Muramoto, S.; Murray, C. B.; Kagan, C. R. Increased Carrier Mobility and Lifetime in CdSe Quantum Dot Thin Films through Surface Trap Passivation and Doping. *J. Phys. Chem. Lett.* **2015**, *6*, 4605—4609.

(44) Cargnello, M.; Diroll, B. T.; Gaulding, E. A.; Murray, C. B. Enhanced Energy Transfer in Quasi-Quaternary Nanocrystal Super-lattices. *Adv. Mater.* **2014**, *26*, 2419—2423.

(45) Kim, W. D.; Chae, W. S.; Bae, W. K.; Lee, D. C. Controlled Vortex Formation and Facilitated Energy Transfer within Aggregates of Colloidal CdS Nanorods. *Chem. Mater.* **2015**, *27*, 2797—2802.